Journal of Applied Fluid Mechanics, Vol. 9, No. 6, pp. 2957-2967, 2016.
Available online at www.jafmonline.net, ISSN 1735-3572, EISSN 1735-3645.
DOI: 10.29252/jafm.09.06.25953

Contribution to the Experimental and Numerical Dynamic Study of a Turbulent Jet Issued from Lobed Diffuser

A. Bennia[1†], L. Loukarfi[1], A. Khelil[1], S. Mohamadi[2], M. Braikia[1] and H. Naji[3]

[1]*Control, Testing, Measurement and Mechanical Simulation laboratory, University Hassiba Benbouali of Chlef, Hay Salem, National Road N° 19, 02000, Algeria.*
[2] *Institute of Physics, USTHB, B.P.32, El-Alia, Bab-Ezzouar, Algiers, Algeria.*
[3]*LGCgE, University of Atois/FSA of Bethume F-62400, France; University Lille Nord of France, F-5900 Lille, France.*

†*Corresponding Author Email: bennia.a_unv@hotmail.com*

(Received December 3, 2015; accepted April 9, 2016)

ABSTRACT

In the present work, we are interested to the experimental and numerical study of the free turbulent lobed jet, used in residential heating and air conditioning. The objective of our study is the improvement of the diffusion performance of the ventilation driving air flow, in the occupancy zone. The experiments have been conducted in a room where the dimensions enables a better execution in the conditions of free and hot vertical jet at unfavorable pushing forces. The installation contains a hot air blowing diffuser oriented from top to bottom. The velocities of the flow were measured by a multi-functional thermo-anemometer. The probe is supported by a stem guided vertically and horizontally in order to sweep a maximum space. Experimentally, we measured the axial and radial velocity field. The dynamics field analysis, show that in the potential core region, the dynamic profiles are more spread at the principal plane and this is due to the widening of the lobes' opening. While, in the transition zone and in the region where the flow is fully developed, these profiles are not influenced by the type of plane and then the jet will be similar to the circular one. Numerically, we used the commercial software Fluent. The obtained numerical results with turbulence method, (RNG k-ε), were in good accordance with the experimental one.

Keywords: Lobed jet; Experimental study; Ventilation; Numerical simulation; Turbulence model.

NOMENCLATURE

D_e	equivalent diameter
G_φ	angular moment
g_i	component of the gravitational vector in the i^{th} direction
G_k	production term of the turbulent kinetic energy
G_x	axial pushing force
H	lobe height
k	turbulent kinetic energy
L	lobe length
P	pressure in the jet cross-section
P_{ij}	production term of the Reynolds stresses
PP	principal plane
Pr_t	turbulent Prandtl number for energy
Re	Reynolds number
S	Swirl number
S_Φ	source term
U_0	mean velocity at the diffuser exit
U_i	velocity at different points of the jet
r/D_e	dimensionless radius (radial direction)
SP	secondary plane
X/D_e	dimensionless height (axial direction) due to the mean velocity gradient
α	inverse effective Prandtl number
β	coefficient of thermal expansion
ε	turbulent kinetic energy dissipation rate
η	mean flow rate deformation
θ_{ext}	exterior angle of the lobes
θ_{int}	interior angle of the lobes
μ	dynamic viscosity
ν	kinematic viscosity
ν_t	turbulent kinematic viscosity
ρ	fluid density
σ_k, σ_ε	turbulent Prandtl numbers associated to k and ε, respectively

1. INTRODUCTION

An important interest is given to the improvement of the mixing process of the turbulent flows by means of the swirling structures generated and intensified artificially, because of their practical aspects. It has been indicated that the mixing process is intimately linked to the transition of the turbulence (Dimotakis 2000), and that the geometry and the initial flow perturbations condition strongly its generation and its transition. Concerning their applications, which are numerous, we can cite: the propulsion force of the aeroplane reactors, the dispersion of pollutant on the industrial sites, in the agglomeration and finally in the transport domain (Meslem *et al.* 2011a). Meslem *et al*. (2010) presented an innovative concept for optimized air diffusion to improve the mixing ventilation in buildings. The used method is a passive control of an air jet through lobed diffusers. All their results led to the same conclusion. In that, the lobed diffuser favors the self-induction as compared to a conventional circular perforated diffuser.

The flow in the near-field of a cross-shaped orifice jet was investigated experimentally by Elhassan *et al.* (2011). The latter found that both the instantaneous entrainment rate and the net volume flux were strongly dependent on the vortical structures present in the flow and particularly at different parts of the Kelvin-Helmholtz vortex ring. Nastase *et al.* (2011) compared the jet flow imparted from an elementary slot with a lobed geometry to a linear slot jet. In their analysis, it was shown that for the elementary slot jets the vortical dynamics in the lobed flow was complex and was governed by large streamwise structures generated by the lobed nozzle lip. This suggests the enhanced performance in terms of induction and mixing.

The passive control permits the improvement of the diffusion of air in buildings (Meslem *et al*. 2012). This consists of the use of, diffusers of lobed geometries. Meslem *et al*. (2014) concluded that when a jet flow is used in mixing process, a large entrainment especially near the jet exit is desired. According to authors, many studies demonstrated the superiority in mixing performance of noncircular jets. noting that the complex manipulations of the jet mixing layer have been achieved with lobed nozzles and extensive previous studies have been conducted on lobed jet mixing flows in the past 30 years at high Reynolds numbers for combustion and aeronautics applications. According to some authors such geometries are attractive for the heating, ventilation and air conditioning (HVAC) field, for their esthetic relatively, low cost and mixing efficiency characteristics.

The lobed nozzle is used to increase the generation of the blowing longitudinal structures. It is suggested in the recent works (Hu *et al.* 2000a) that a lobed jet in the form of marguerite with 6 lobes, having an inclination of the boundary, constitutes an extraordinary mixing tool in the region of potential core. It is noticed that the induction phenomenon is dominated by the presence at the summits of the nozzle lobe's of 6 pairs of contrarotating longitudinal structures where the size is compared to that of the lobe. Large secondary structures develop in the troughs of the lobed nozzle (Meslem *et al.* 2011 a ; Elhassan *et al.* 2011). The phenomenon of crossing axes participates to the increase in the induction performance of the lobed jet. It is also possible to optimize the geometry of the elementary lobed orifice of the diffuser, in order to improve the global performance. Yuan (2000) is among the firsts who were interested in the effect of the circular lobed nozzle of different forms and at variable number of lobes. To the works of Yuan (2000) on the lobed jets, were added those of Hu *et al.* (2000b, 2001). Contrary to the precedent boundary conditions, the air jet, here, is free and diffused in the air at rest. It is noticed that for these experiments, the initial Reynolds number Re_{0C}, based on the equivalent diameter of the nozzle and the central blowing velocity U_{0C} of 1.2m/s, is equal to 3000 (Hu *et al.* 2000b, 2001).

Dia (2012) indicates that in the fully developed region, the velocity profiles and the turbulence obey the similitude laws. Further, the turbulent energy is concentrated around the axis of the mixing boundary where the radial velocity gradients are maximums. It is identified that the swirls centered on the axis of the mixing boundary where the size increases with the longitudinal distance X.

Bennia *et al.* (2015) presented also a comparative study of the performance of different nozzle geometries. By the analysis of the jet axial velocity profiles, the comparison of the lobed jet using various lobe geometries shows that a diffuser with inclined lobes homogenize the air flow in the experimental room relatively better than a lobed diffuser at right section.

Meslem *et al.* (2011b) studied the performances of the three turbulence models: the *k-ω* SST, RSM and the *k-ε* standard. She noted that none of the turbulence models can predict correctly all the flow characteristics. However, it has been shown that, among the studied viscous models, the *k-ω* SST turbulence model is capable to predict properly the jets interaction, the global dynamic expansion and the entrainment of the ambient air for the volume flow issued from a lobed diffuser.

The principal objective of this work is to study, the distribution of the velocities, first experimentally and then numerically, for a jet configuration from a lobed diffuser. This type of flow has been studied in sight of its application to the ventilation of residences.

2. TEST EXPERIMENTAL ASSEMBLY AND WORKING CONDITIONS

The experimental assembly is essentially designed to generate an air jet from a lobed diffuser. The experiments have been carried out in a room of a length of 3,0*m*, a width of 2,5*m* and a height of 2,5*m*. These dimensions enable to carry out tests at a vertical free and hot jet conditions with unfavorable pressure forces. The Archimedes number of the jet is conserved during the experiments. The installation is composed of a chassis on which the blowing device

is fixed (Fig. 1). This latter contains a hot air blowing diffuser oriented towards the bottom. The flow velocities and temperatures are measured with a multifunctional thermo- anemometer (Braikia *et al.* 2012). The probe is supported by a stem guides vertically and horizontally in order to sweep the maximum space. The velocity U_i at different points is taken simultaneously.

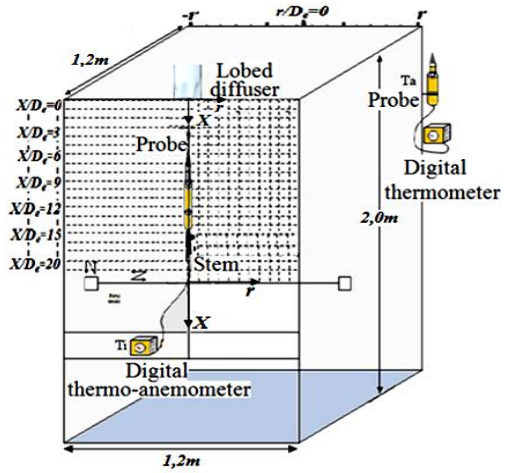

Fig. 1. Schemtic description of the experimental installation.

Figure 2 shows the lobed nozzle which is composed of 6 lobes inclined with an angle θ_{int} of 0° from the blowing plane. These troughs are inclined with an angle θ_{ext} of 22° towards the inside. The nozzle is of 0.046m equivalent diameter and a length of 0.09m. The lobes are with more wide openings**,** the width of each is 0.006m and its height is 0.01m. The jet air initial velocity at the blowing orifice is 8 m.s^{-1}.

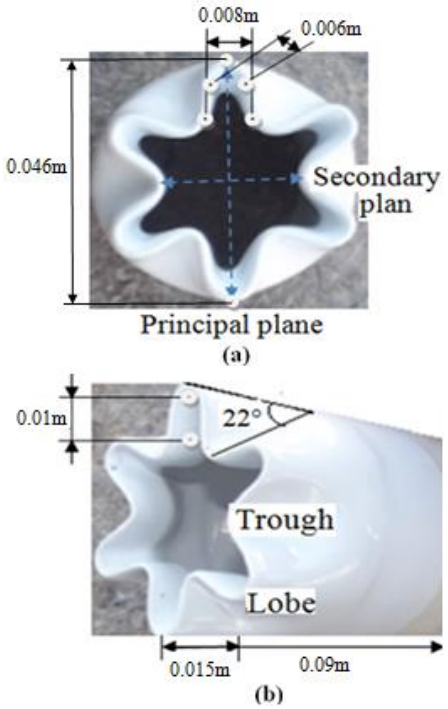

Fig. 2. "a), Geometry of the blowing plane (YZ) ,"b) Photography of a lobed nozzle.

3. MEASUREMENT ERRORS ESTIMATION

The reduced dimensionless axial velocity (U_r) is obtained with reference to the maximal velocity at the outlet of the blowing orifice U_0.

$$U_r = \frac{U_i}{U_0} \tag{1}$$

$$\frac{\Delta U_r}{U_r} = \frac{\Delta U_i}{U_i} + \frac{\Delta U_0}{U_0} \tag{2}$$

The uncertainty associated to the velocity measurements was estimated to be less than 5 %.

4. RESULTS AND DISCUSSION

4.1 Experimental Axial Velocity Profile of a Free Lobed Jet

The reduced velocity profile (U_r) of a lobed air jet is shown below.

Figure 3 shows the axial distribution of the reduced velocity (U_r) on an axial distance of 20 equivalent diameters for a single lobed jet. The axial velocity distribution profile illustrates the curve of the Gaussian distribution throughout the jet which proves that stability of the velocity appears when we move away from the blowing orifice.

We noticed that the axial velocity reached its maximum at 1D_e, very near to the blowing orifice then they decrease rapidly to attain nearly the 2/3 of its initial value at 7D_e. From the axial station 7D_e to 15D_e, we observe a second slope which is less accentuated than the first. Beyond the 15 equivalent diameters, the velocity's intensity becomes weak and regular along the flow. This result enables us to quantify the relative importance of the inclination of the trough in relation to the lobed geometry of the bowing plane. This rapid decrease of the axial velocity explains the transfer of energy to the radial direction.

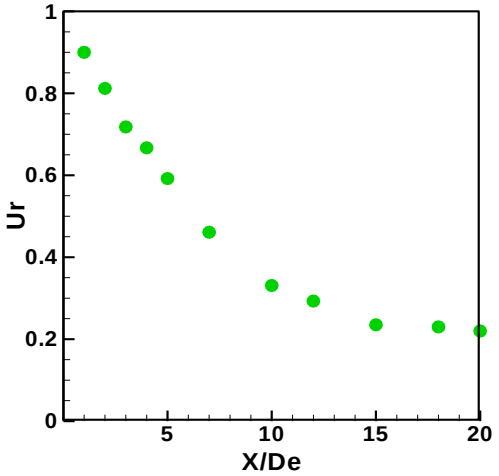

Fig. 3. Axial velocity profiles of a free lobed air jet.

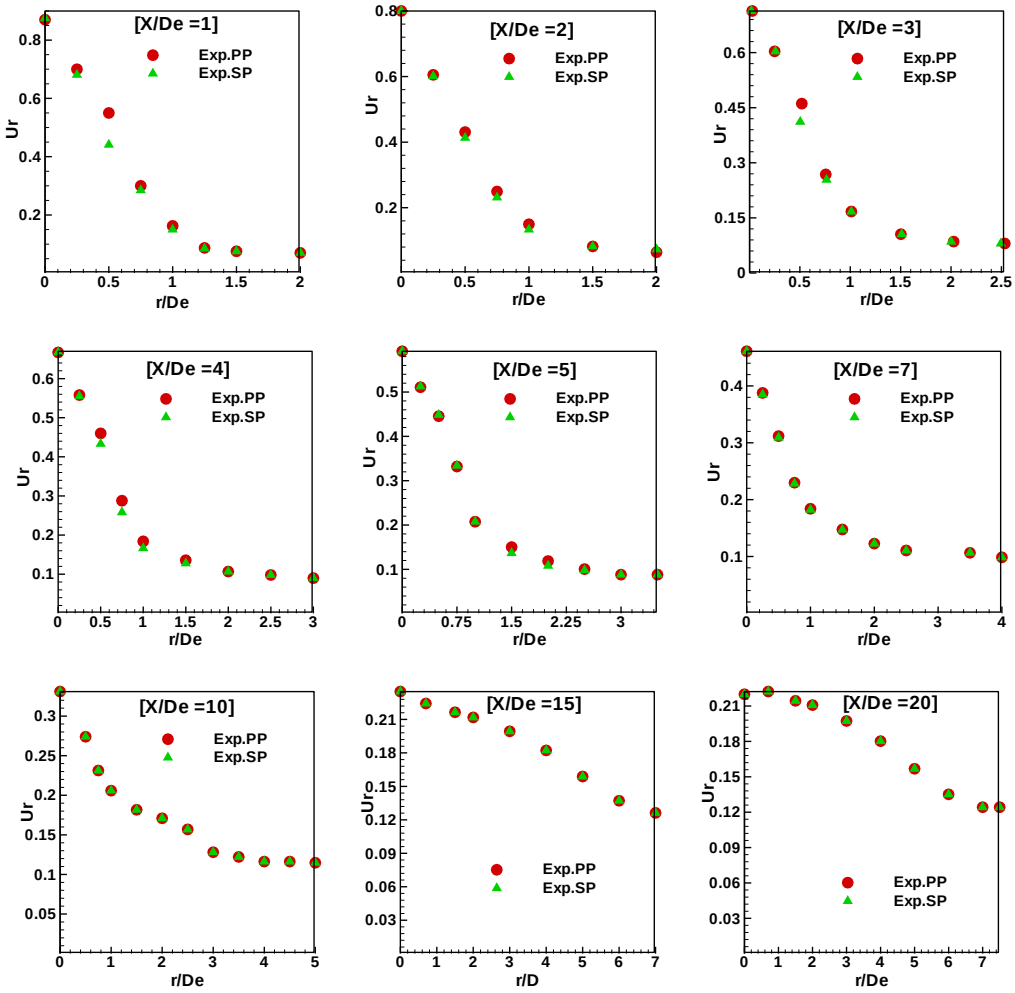

Fig. 4. Radial velocity profiles of a free lobed jet.

4.2 Experimental Radial Velocity Profiles of a Free Lobed Jet

Figure 4 shows the radial velocity profiles for different stations (X/D_e=1, 2, 3, 4, 5, 7, 10, 15 and 20).

4.2.1 Principal and Secondary Planes

Figure 4 shows the compared radial velocity profiles in the principal and secondary planes for a free lobed jet.

According to the radial velocity profiles relating to principal and secondary planes, for different axial stations, represented on Figure 4, we can notice that:

In the symmetry plane of the studied configuration (Fig. 4), the velocity reaches its maximum near the jet axis, then diminishes radially. We notice also that the velocities are stabilized at the stations distant from the jet axis, for the two planes.

From the axial station $1D_e$ till the $7D_e$ *(the potential core region*), the secondary plane gives a weak radial spreading of the velocities contrary to the principal plan.

At the end of the explored zone $X=7D_e$ (*the region, where the flow is fully developed*), the two axes are rejoined, which let us presuming that the lobed jet become circular and that is why the velocity profiles are identical. It is the same for the radial spreading for the two planes principal and secondary.

5. NUMERICAL PROCEDURE

5.1. Introduction

We configured the geometry of the studied case and generated its meshing. Also we incorporated the boundary conditions by means of the meshing software Gambit and the solver Fluent (v.6). We used the finite volumes method. In order to improve the previsions of the turbulent methods, we tested four turbulence models *k*–ε standard and RNG, *k*-*ω* SST and the de Reynolds stress turbulence model RSM in order to opt for the more adequate model relating to this type of flow.

5.2 Finite Volumes Method

The principle of this method stands on a discretization technique, which converts the partial differential equations to algebraic equations, which can, then, be solved numerically (Bennia *et al.* 2014). It is distinguished by the reliability of their results; its

adaptation to the physical problems its ability to treat complex geometry. It ensures the conservation of the mass and the moment and all transportable scalars on each control volume in the calculation domain.

5.3 Mathematical Model

The equations governing the flow are the continuity and Navier-Stokes, which express the mass, moment and energy conservation (Bennia *et al.* 2014).

- Continuity equation:

$$\frac{\partial u}{\partial x}+\frac{\partial v}{\partial y}+\frac{\partial w}{\partial z}=0 \tag{3}$$

- Navier-Stokes equations (moment):

$$\rho\frac{\partial(U_iU_j)}{\partial x_j}=-\frac{\partial P}{\partial x_i}+\frac{\partial}{\partial x_j}\left[\mu\left(\frac{\partial U_i}{\partial x_j}+\frac{\partial U_j}{\partial x_i}\right)-\rho\overline{U_iU_j}\right] \tag{4}$$

The solution of the system of steady-state equations previously obtained necessitates the incorporation of boundary conditions for each variable.

5.4. Classification of Turbulence Models

5.4.1. Turbulence Model (*k*-ε) Standard

The (*k*-ε) turbulence model is one in which the Reynolds stresses are supposed to be proportional to the mean velocity gradient, with a constant of proportionality representing the turbulent viscosity μ_t.

This hypothesis, called the "Boussinesq" hypothesis, give the following expression for the tensor of Reynolds stresses (Pratte *et al*. 1972):

$$\rho\overline{\acute{u}_i\acute{u}_j}=\rho\frac{2}{3}k\delta_{ij}-\mu_t\left(\frac{\partial u_i}{\partial x_j}+\frac{\partial u_j}{\partial x_i}\right)+\frac{2}{3}\mu_t\frac{\partial u_i}{\partial x_i}\delta_{ij} \tag{5}$$

Where *k* is the turbulent kinetic energy defined by:

$$k=\frac{1}{2}\sum_i\overline{\acute{u}_i^2} \tag{6}$$

The turbulent viscosity μ_t is supposed proportional to the product of the turbulent velocity and the length scales. In the *k*-ε model, these velocity and length scales, are obtained from the two parameters, the kinetic energy *k* and the rate of dissipation ε. Therefore μ_t can be expressed by the following relation:

$$\mu_t=\rho C_\mu\frac{k^2}{\varepsilon} \tag{7}$$

With C_μ =0.09 (empirical constant).

The values of *k* and ε required in the equation are obtained by solving the following conservation equation:

$$\frac{\partial}{\partial t}(\rho k)+\frac{\partial}{\partial x_i}(\rho u_i k)=\frac{\partial}{\partial x_j}\left[\left(\mu+\frac{\mu_t}{\sigma_k}\right)\frac{\partial k}{\partial x_j}\right]+G_k+G_b-\rho\varepsilon+S_k \tag{8}$$

$$\frac{\partial}{\partial t}(\rho\varepsilon)+\frac{\partial}{\partial x_i}(\rho u_i\varepsilon)=\frac{\partial}{\partial x_j}\left[\left(\mu+\frac{\mu_t}{\sigma_k}\right)\frac{\partial\varepsilon}{\partial x_j}\right]+\mathrm{C}_{1\varepsilon}\frac{\varepsilon}{k}(G_k+\mathrm{C}_{3\varepsilon}G_b)-\mathrm{C}_{2\varepsilon}\rho\frac{\varepsilon^2}{k}+S_\varepsilon \tag{9}$$

With

$\mathrm{C}_{1\varepsilon}=1.44$ and $\mathrm{C}_{2\varepsilon}=1.92$; empirical constants.

$\sigma_k=1.0$ and $\sigma_\varepsilon=1.3$ Prandtl numbers for *k* and ε respectively.

S_k and S_ε are source terms for *k* and ε respectively.

G_k: represents the generation of the turbulent kinetic energy due to mean velocity gradient.

$$G_k=\mu_t\left(\frac{\partial u_j}{\partial x_i}+\frac{\partial u_i}{\partial x_j}\right)\frac{\partial u_j}{\partial x_i} \tag{10}$$

G_b: coefficient of the generation of the turbulence due to the entrainment.

$$=-g_i\frac{\mu_t}{\rho\sigma_h}\frac{\partial\rho}{\partial x_i} \tag{11}$$

5.4.2. Turbulence Model *k*-ε RNG

In the flows with high rate of stresses the model RNG predicts a low turbulent viscosity (high rate of dissipation ε and a low production of turbulence *k*) comparing to the standard model (Choudhury 1993).

Though the RNG *k*-ε model has been discovered to be more convenient than the standard model for the flows with large curvature of stream lines, it is not yet validated intensively by the researchers as much as the *k*-ε model.

Transport equations: The model is based on the transport equations of a similar form to that of the standard model:

$$\frac{\partial}{\partial x_i}(\rho k\overline{U}_\iota)=\frac{\partial}{\partial x_j}\left[\alpha_k\mu_{eff}\frac{\partial k}{\partial x_j}\right]+G_k-\rho\varepsilon \tag{12}$$

$$\frac{\partial}{\partial x_i}(\rho\varepsilon\overline{U}_\iota)=\frac{\partial}{\partial x_j}\left[\alpha_\varepsilon\mu_{eff}\frac{\partial\varepsilon}{\partial x_j}\right]+C_{1\varepsilon}\frac{\varepsilon}{k}(G_k)-R_\varepsilon-C_{2\varepsilon}\rho\frac{\varepsilon^2}{k} \tag{13}$$

: inverse effective Prandtl number for *k*

α_ε: inverse effective Prandtl number for ε

Modeling of the effective viscosity:

$$d\left(\frac{\rho^2k}{\sqrt{\varepsilon\mu}}\right)=1.72\frac{\hat{v}}{\sqrt{\hat{v}^3-1+C_v}}d\hat{v} \tag{14}$$

Where:

$C_v\approx 100$ and $\hat{v}=\frac{\mu_{eff}}{\mu}$

In the case of a high Reynolds number (Eq. 7), but in the RNG model C_μ=0,085.

The modification of the RNG for the swirling:

$$\mu_t = \mu_{t0} f\left(\alpha_s, \Omega, \frac{k}{\varepsilon}\right) \quad (15)$$

μ_{t0} : the value of the turbulent viscosity calculated without swirling

: Swirling characteristic number

α_s : Swirling constant, equals to 0.07.

5.4.2.1. Calculation of the Effective Inverse Prandtl number

α_k, : are calculated by means of the following formula :

$$\left|\frac{\alpha - 1.3929}{\alpha_0 - 1.3929}\right|^{0.6321} \left|\frac{\alpha + 2.3929}{\alpha_0 + 2.3929}\right|^{0.3679} = \frac{\mu_{mol}}{\mu_{eff}} \quad (16)$$

Where:

In the case of the RNG ***k-ε*** Model, $\boldsymbol{\alpha}=\frac{1}{Pr_t}$.

α_0=1. In the case of very high Reynolds number: $\mu_{mol}/\mu_{eff} \ll 1$ and $\alpha_k=\alpha_\varepsilon$=1.393.

5.4.2.2. Calculation of the R_ε Term:

The important difference between the RNG and the standard models resides in the term ε added to the equation given by:

$$R_\varepsilon = \frac{C_\mu \eta^3 (1 - \frac{\eta}{\eta_0})}{1 + \beta\eta^3} \frac{\varepsilon^2}{k} \quad (17)$$

Where: $\eta = Sk/\varepsilon$, $\eta_0 = 4.38$, $= 0.012$

Using the (Eq.7), the (Eq.13) becomes:

$$\frac{\partial}{\partial x_i}(\rho\varepsilon\overline{U_i}) = \frac{\partial}{\partial x_j}\left[\alpha_\varepsilon \mu_{eff} \frac{\partial \varepsilon}{\partial x_j}\right] + C_{1\varepsilon}\frac{\varepsilon}{k}(G_k) - C_{2\varepsilon}^{*}\rho\frac{\varepsilon^2}{k} \quad (18)$$

Where $C_{2\varepsilon}^{*}$ is given by:

$$C_{2\varepsilon}^{*} = C_{2\varepsilon} + \frac{C_\mu \rho \eta^3 (1 - \frac{\eta}{\eta_0})}{1 + \beta\eta^3} \quad (19)$$

The constants of the model are given in following table:

Table 1 RNG *k*- *ε* model Constants

C_μ	$C_{1\varepsilon}$	$C_{2\varepsilon}$	σ_ε	η_0	β
0.085	1.42	1.68	0.7179	4.38	0.015

5.4.3. Reynolds Stress Model (RSM)

In this model the Reynolds stresses are calculated according to their proper transport equations and the (isotropic) turbulent viscosity concept is not required. Thus this model involves the individual calculation of each stress $\overline{u_\iota u_j}$. These equations are used to close the averaged Reynolds equation system for the transport of the moment equation (Choudhury 1993). Simplifying hypothesis for the modeling of the unknown terms is necessary and the selected propositions are briefly presented:

The transport equations of the Reynolds stresses are written in the fluent code as follows:

$$\underbrace{\frac{\partial}{\partial x_k}\left(\rho U_k \overline{u_\iota u_j}\right)}_{1} = \underbrace{-\frac{\partial}{\partial x_k}\left[\rho\,\overline{u_\iota u_j u_k} + p\left(\overline{\delta_{kj} u_\iota + \delta_{\iota k} u_j}\right)\right]}_{2} + \underbrace{\frac{\partial}{\partial x_k}\left[\mu \frac{\partial}{\partial x_k}\left(\overline{u_\iota u_j}\right)\right]}_{3} - \underbrace{\rho\left[\overline{u_\iota u_k}\frac{\partial U_j}{\partial x_k} + \overline{u_j u_k}\frac{\partial U_i}{\partial x_k}\right]}_{4} + \underbrace{p\left(\frac{\partial u_i}{\partial x_j} + \frac{\partial u_j}{\partial x_i}\right)}_{5} - \underbrace{2\mu\,\overline{\frac{\partial u_\iota}{\partial x_k}}\overline{\frac{\partial u_j}{\partial x_k}}}_{6} \quad (20)$$

1: c_{ij} ≡ convection

2: $D_{T,\,ij}$ ≡ turbulent diffusion

3: $D_{L,\,ij}$ ≡ molecular diffusion

4: P_{ij} ≡ stress production term

5: ϕ_{ij} ≡ strain rate

6: ε_{ij} ≡ dissipation

We supposed that the effects of buoyancy and compressibility are neglected since the studied case is steady and without heat transferred.

$$\underbrace{D_{T,ij} = C_s \frac{\partial}{\partial x_k}\left(\rho k \frac{\overline{u_k u_1}}{\varepsilon}\frac{\partial \overline{u_i u_j}}{\partial x_1}\right)}_{\text{Turbulent diffusif transport}} \quad (21)$$

Because of the instability of calculation with this model, a simplification has been introduced, and this isotropic diffusive term gives good results for anisotropic cases.

$$D_{T,ij} = \frac{\partial}{\partial x_k}\left(\frac{\mu_t}{\sigma_k}\frac{\partial \overline{u_i u_j}}{\partial x_k}\right) \quad (22)$$

k : is the Von Karman constant .

Generally, the relation of the turbulent kinetic energy is given by:

$$k = \frac{1}{2}\overline{u_\iota u_\iota} \quad (23)$$

The dissipation tensor is modeled as follows:

$$\varepsilon_{ij} = \frac{2}{3}\delta_{ij}(\rho\varepsilon) \quad (24)$$

The dissipation is calculated by means of a transport equation similar to that of the *k*-*ε* model:

$$\rho\frac{D\varepsilon}{Dt} = \frac{\partial}{\partial x_j}\left[\left(\mu + \frac{\mu_t}{\sigma_t}\right)\frac{\partial \varepsilon}{\partial x_j}\right] + C_{\varepsilon 1}\frac{1}{2}[P_{ii}]\frac{\varepsilon}{K} - C_{\varepsilon 2}\rho\frac{\varepsilon^2}{k} \quad (25)$$

σ_ε = 1.0, $C_{\varepsilon 1}$ = 1.44, $C_{\varepsilon 2}$ = 1.92

If the RSM model is used, the Reynolds stress values at the inlet are not implemented; they are determined approximately by specific values of *k*.

The turbulence is supposed isotropic and we can write:

$$\overline{u_i u_j} = \frac{2}{3}k \;\; pour\; i = j$$

$$\overline{u_i u_j} = 0.0 \;\; pour\; i \neq j$$

Near the boundaries, the software Fluent apply the explicit boundary layers for the Reynolds stresses using the logarithmic law, assuming the equilibrium state and neglecting the convection and the diffusion in the stresses transport equation.

5.4.4. The SST *k* -*ω* Turbulence Model

Several approaches have been proposed in order to correct the boundary conditions of *k* and *ω*. The SST *k*-*ω* is one of the more used turbulence model (Menter 1993). This model uses a function F_1 which enables us to pass from the *k*-*ω* model near the wall to the *k*-*ε* model fare away from it.

$$\frac{\partial(k)}{\partial t} + < u_j > \frac{\partial k}{\partial x_j} = \frac{\partial}{\partial x_j}\left[\left(\nu + \frac{\nu_t}{\sigma_k}\right)\frac{\partial k}{\partial x_j}\right] - \beta^* k\omega_k + \nu_t S^2 \quad (26)$$

$$\frac{\partial \omega}{\partial t} + < u_j > \frac{\partial \omega}{\partial x_j} = \frac{\partial}{\partial x_j}\left[\left(\nu + \frac{\nu_t}{\sigma_\omega}\right)\frac{\partial \omega}{\partial x_j}\right] - \gamma S^2 - \beta f_\beta \omega^2 + 2\sigma_{\omega 2}(1 - F_1)\frac{1}{\omega} \quad (27)$$

The coefficients $\phi \in \{\sigma k, \sigma\omega, \gamma, \beta\}$ of the model are interpolated using the following formula:

$$\phi = F_1\phi_1 + (1 - F_1)\phi_2 \quad (28)$$

The coefficients ϕ_1 are those of the *k*-*ω* model (boundary layer: viscous sub-layer, buffer region, logarithmic layer) and the coefficients ϕ_2 are those of the *k*-ε model (outside the boundary layer). The function F_1 equals to 1 in the boundary layer and 0 outside it. Further, in this model, the Bradshaw (Bradshaw 1987) hypothesis is used in order to limit the turbulent viscosity in the regions with adverse pressure gradients:

$$\nu_t = \frac{a_1 k}{\max(a_1\omega; F_2\bar{\Omega})} \quad (29)$$

$$\bar{\Omega} = \sqrt{2\Omega : \Omega} \quad avec$$

$$\Omega_{ij} = \frac{1}{2}\left(\frac{\partial < u_i >}{\partial x_j} - \frac{\partial < u_j >}{\partial x_i}\right) \quad (30)$$

Where:

a is the Bradshaw constant (Bradshaw 1987) (a_1=0.31). The Bradshaw correction "Bradshaw (1987)" is applied in the boundary layer (where F_2= 1), and outside the boundary layer we used the relation $\nu_t = k/\omega$ (where F_2= 0).

5.5. Boundary Conditions

We presented the boundary conditions of the domain according to the considered boundary. Also, for each type of boundary conditions, there are several variants of conditions. For the studied case, the boundary conditions are presented in the figure below. The room dimensions are very large compared to those of the zone of air diffusion.

The boundary conditions for the turbulence models *k*-*ω* SST, *k*-*ε* standard, RNG *k*-*ε* and the RSM model are as follows:

- Inlet velocity: 8 (m/s)
- Turbulence intensity : 5 (%)
- Relaxation factors : Pressure = 0.3, Density = 0.9, Energy = 0.9, Moment = 0.6, body forces = 0.9, Turbulent kinetic Energy = 0.7, Specific Dissipation Rate = 0.7, Turbulent Viscosity = 0.9.
- Convergence critirea : Energy =$10^{-7,}$ other parameters =10^{-4}.
- Reynolds Number : $R_{eynolds}$ = 1.8330*10^4.
- Pressure : Standard.

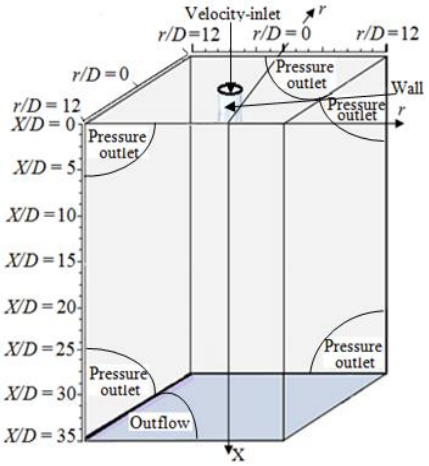

Fig. 5. Calculation domain and working stress.

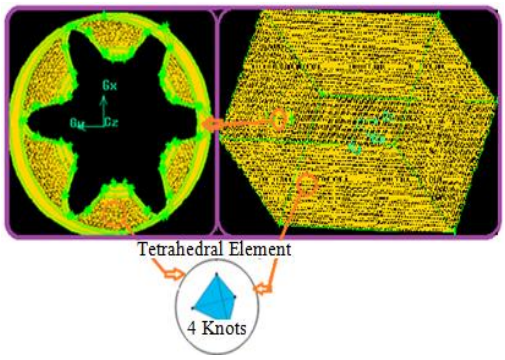

Fig. 6. Meshing of the calculation domain.

Table 2 Tested meshes

Meshing Number	Cell number
Mesh1	633268
Mesh2	1128214
Mesh3	1702062
Mesh4	2326082
Mesh5	3301991
Mesh6	4089508

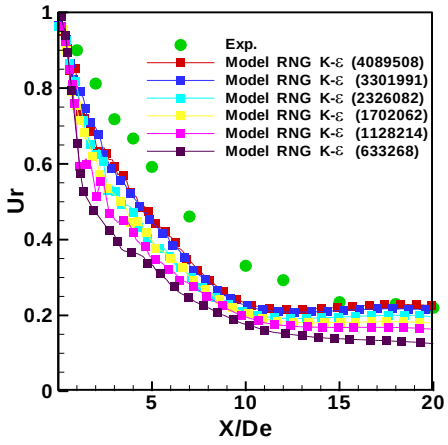

Fig. 7. Independence of the solution from the meshing, for the axial velocity.

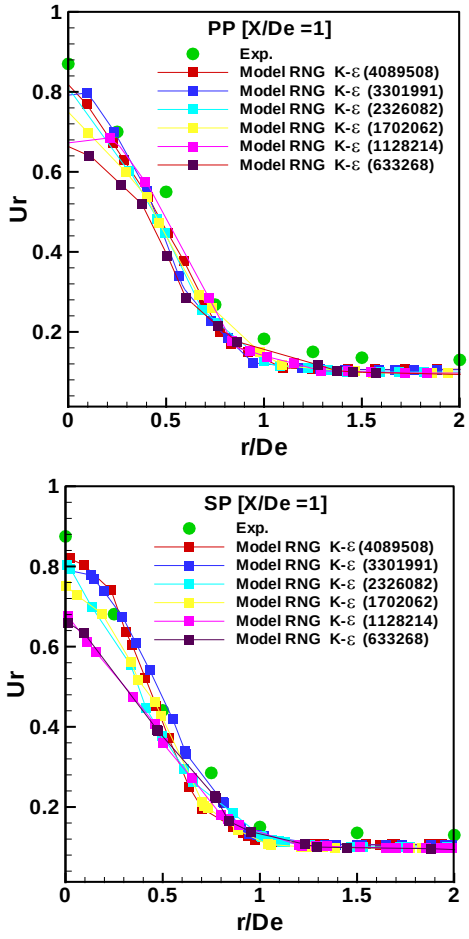

Fig. 8. Independence of the solution from the meshing for the radial velocity at X/D_e=1 in the principal and secondary planes.

5.4. Effect of Meshing

For our tridimensional study, we exposed the simulation results obtained by means of the software «Fluent» and the the meshing software Gambit. For the studied case, we optimised, the mesh convenient for our study.The results have been validated by comparison with those obtained experimentally.

One turbulence model which is the RNG *k-ε*, has been tested with several meshing in order to study their effects.

From these figures, we noticed that from the meshing 5 (Table 2), the axial and radial velocity profiles do not vary with the meshing, that is why we executed our simulations with only this meshing.

5.5. Results Validation

5.5.1. Reduced Axial Velocity Profiles for a Lobed Jet

Figure 9 presents a comparison between the experimental and numerical results relating to the reduced axial velocity (U_r) at different stations. The numerical results are obtained by means of the four turbulence models: k-*ω* SST, k-*ε* standard, RNG k-*ε* and the RSM.

Concerning the velocities, Figure 9 shows that the velocities, predicted with the turbulence models RNG k-*ε*, k-*ε* standard and the RSM, are, in general, in good accordance with the experiment.

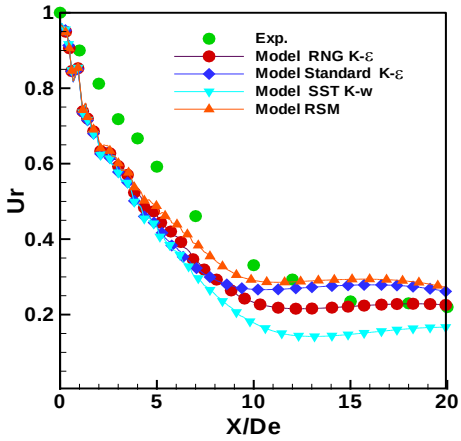

Fig. 9. Comparison of the experimental and numerical velocity profile in the axial direction.

Starting from the station X/D_e=5, the k-*ω* SST model gives a similar form presenting a certain discrepancy with the experimental values. Also, the RNG k-*ε* turbulence model validates correctly the axial velocity profile.

The axial velocities predicted with the RNG k-*ε*, k-*ε* standard and RSM turbulence models are in good accordance with the experimental values for the prediction of the blowing mean flow near the exit, which let us suggesting that these models treat correctly the flow interaction with the diffuser. All the turbulence models fail to predict the evolution of the axial velocity (U_r), in the entire explored domain at the same time. The length of the potential core close to the experiment is given by the RNG k-*ε* model. Fig. 9 indicates that among the turbulence models, under evaluation, the RNG k-*ε* model is the nearest to the experimental values and predicts satisfactory the evolution of the axial velocity of the jet. The k-*ω* SST turbulence model, predicts unsatisfying similar evolutions of the dynamic grandeurs.

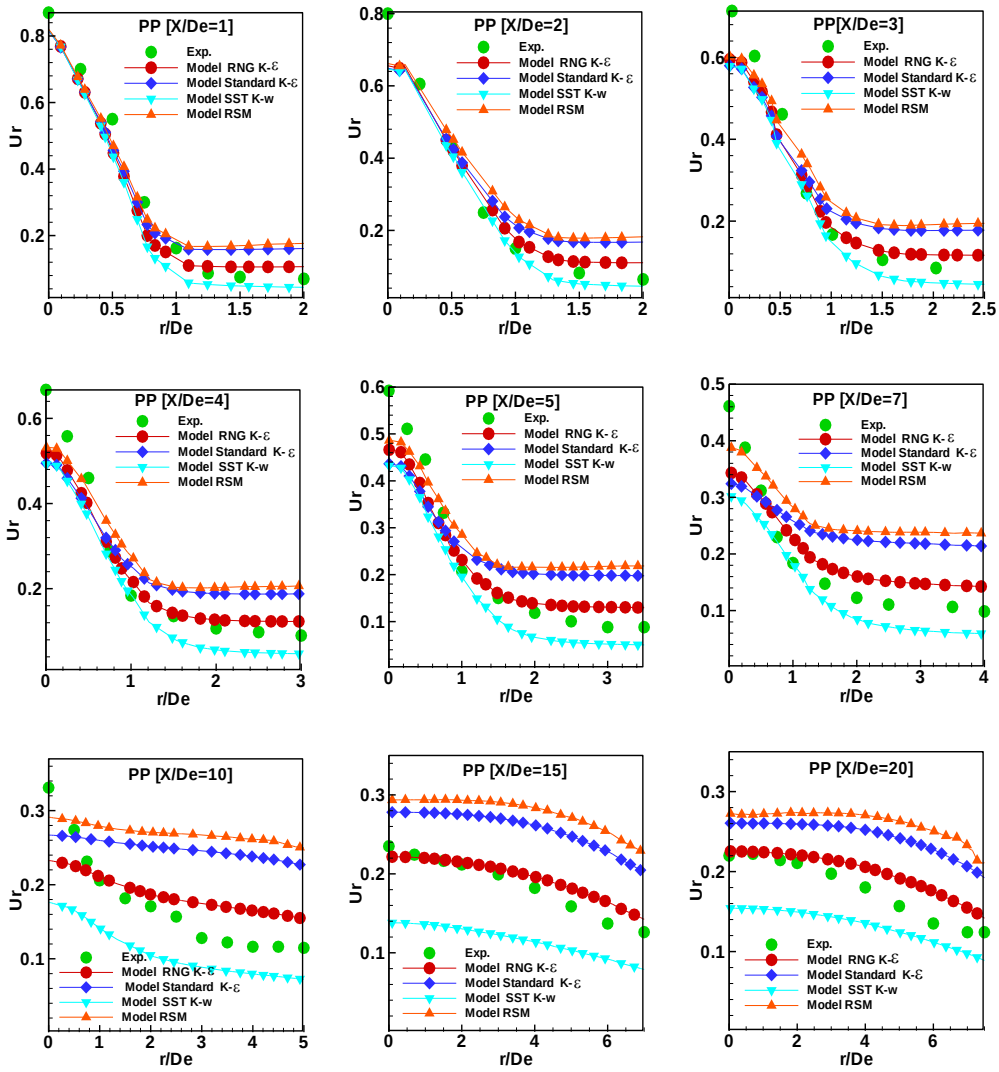

Fig. 10. Comparison of the experimental and numerical radial velocity profiles (principal plane).

5.5.2. Reduced Radial Velocity Profiles of a Lobed Jet

5.5.2.1. Reduced Radial Velocity Profils in the Principal Plane

Figs. 10 and 11 show the radial velocity profiles, for the principal and secondary planes. The four numerical profiles based on the RNG k-ε, k-ε standard, k-ω SST and RSM turbulence models are compared to the expérimental results for the stations (X/D_e=1, 2, 3, 4, 5, 7, 10, 12, 15 et 20).

The radial velocity profiles issued from the k-ε standard and RSM turbulence models deviates from the experimental values. Even if the k-ω SST model approaches the experimental result, it appears that the RNG k-ε turbulence model validates better than the other three models, the experimental results, for both principal and secondary planes.

5.5.3. Velocity Contours

From the velocity fields obtained according to the turbulence model RNG k-ε (Fig. 12), the software «Fluent» enables to visualize the velocity contours, this is done, for the principal plane (Fig.12 a)) and for the secondary plane (Fig.12 b)).

The velocities of the lobed jet decrease through the flow particularly in the potential core region. This velocity behavior, are validated by the experimental results at different axial and radial distances for the principal and secondary planes. By analyzing these figures we remark that the radial velocities are not homogeneous near the blowing device, they start to be homogenized after a certain axial and radial distance from the surface of the outlet jet. This behavior confirms the influence of both the lobes form and troughs that enable a relative jet expansion in the principal plane comparing to the secondary , this is done, before the station X/D = 7 (potential core region). Beyond this value (the region, where the flow is fully developed), the lobed jet behaves like a circular one.

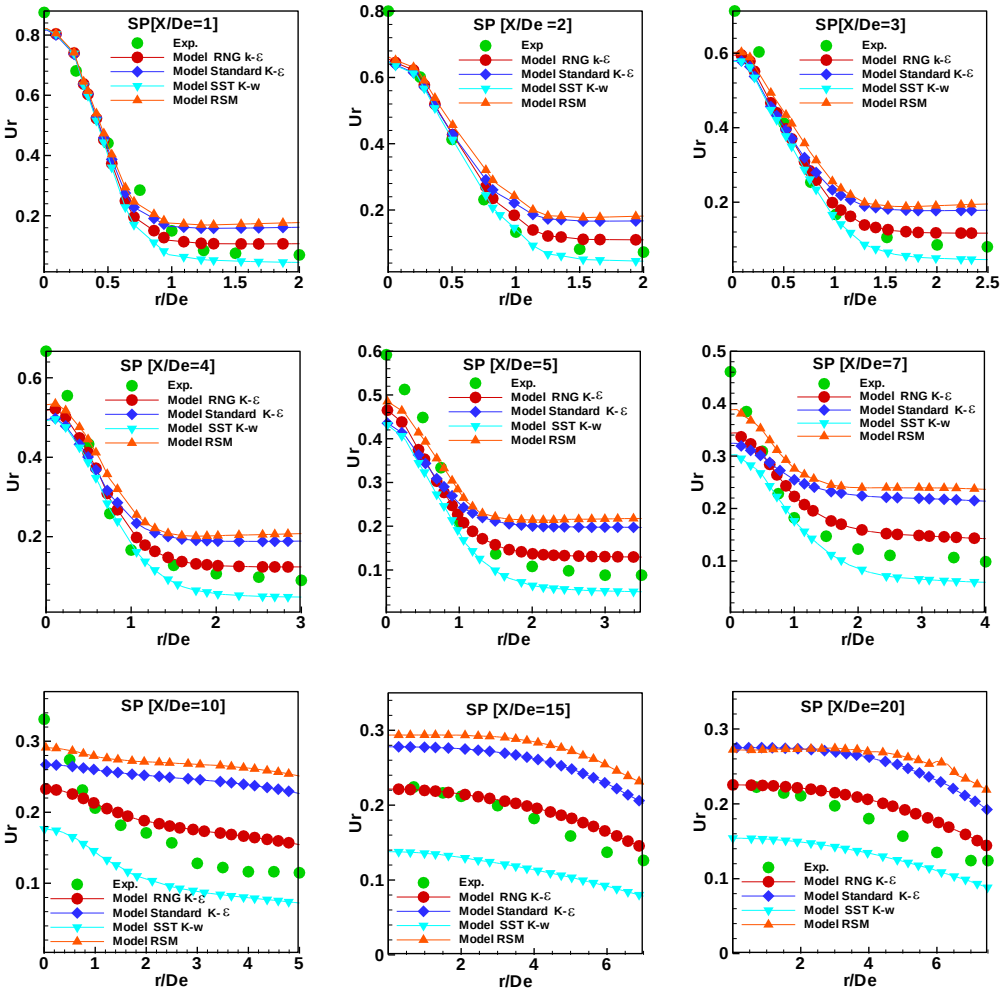

Fig. 11. Comparison of the experimental and numerical radial velocity profiles (secondary plane).

6. CONCLUSION

This study of the jet produced by diffuser equipped with lobes has been done in order to test their performances in terms of homogenization of this type of environment. By comparison to the circular jet, the lobed one is characterized by a principal and a secondary plane. It has an important transversal shearing due to the inclination of the trough. To ensure the occupant's comfort, the blowing velocities should be homogeneous, which is not guaranteed by simple air diffuser of the classical terminal units. In the potential core region, the dynamic profiles are more spread at the principal plane and this is due to the fact of the more widen opening of the lobes. In the transition zone and in the region where the flow is fully developed, these profiles are not influenced by the type of plane and then the jet will be similar to the circular one.

Among the tested models, only the RNG k-ε and SST k-ω that are in good accordance with the experimental results for the prediction of the mean flow around the axial jet, which let us suggesting that these models take into account the interaction of the flow with the diffuser for both the principal and secondary planes.

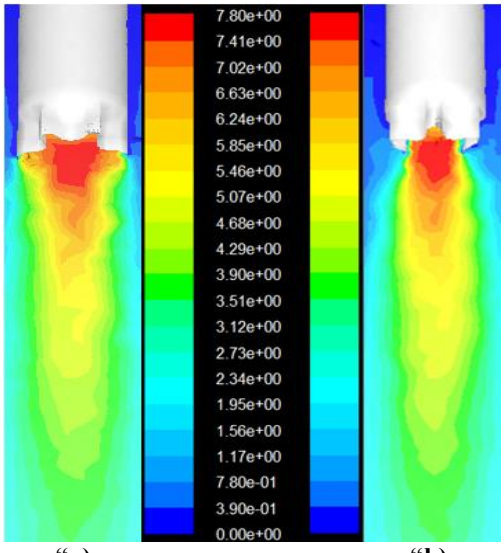

"a) **"b)**

Fig. 12. Velocity contours,"a) principal plane,"b) secondary plane.

The confrontation of the lobed jet simulated with the experiment, reveals that none of the four evaluated

turbulence models enables the prediction, of the entire dynamic characteristics, in the same time. It is also shown that the good prediction of the flow on a plane does not ensure it on the entire flow. Among the evaluated turbulence models, only the RNG k-ε one that gives results close to these issued from the experiment and predicts in a satisfactory way the evolution of the jet radial velocities. The other turbulence models, the k-ε standard and RSM, predict unsatisfying velocities evolutions.

REFERENCES

Bennia, A., and S. Rahal (2014). *Numerical study of natural convection in a vertical rectangular enclosure simulating a thermosyphon.* Editions Universitaires Europeennes, saarbrücken (Germany), 1-124.

Bennia, A., L. Loukarfi, M. Braikia, A. Khelil, and H. Naji, (2015). Etude expérimentale d'un jet turbulent à diffuseur muni de lobes : Application au confort dans les locaux à usage d'habitation, *Nature & Technologie. A-Sciences fondamentales and Engineering* 13, *54 -58.*

Bradshaw, P. (1987). Turbulent secondary flows. *Annual Review of Fluid Mechanics* 19(1), 53–74.

Braikia, M., L. Loukarfi, A. Khelil and A. Naji (2012). Improvement of thermal homogenization using multiple swirling jets. *Thermal science* 16(1), 239-250.

Choudhury, D. (1993). Introduction to the Renormalization Group Method and Turbulence Modeling. *Fluent Inc. Technical Memorandum*, 107.

Dia, A. (2012). *Numerical simulation of lobed air jets for the optimization of Air Diffusion Terminal Units for buildings. Ph. D. thesis, University of La Rochelle, France.*

Dimotakis, P. E. (2000). The mixing transition in turbulents flows. *Journal of Fluid Mechanics* 409, 68-69.

Elhassan, M., A. Meslem and K. Abed-Meraïm (2011). Experimental investigation of the flow in the near-field of a cross-shaped orifice jet. *Physics of Fluids* 23, 16.

Hu, H. and *et al*. (2000a). Research on the Vertical and Turbulent Structures in the lobed jet Flow Using Laser Induced Fluorescence and Particle Image Velocimetry Techniques. *Measurement Science and Technology* 11, 698-711.

Hu, H., T. Kobayashi and N. Taniguchi (2001). A study on a lobed jet mixing flow by using stereoscopic particle image velocimetry technique. *Physics of* Fluids 13, 25-34.

Hu, H., T. Kobayashi, T. Saga, S. Segawa and N. Taniguchi (2000b). Particle image velocimetry and planar laser-induced fluorescence measurements on lobed jet mixing flows. *Experiments in Fluids* 29, 141–157.

Menter, F. R. (1993). Zonal two equation k-*w* turbulence models for aerodynamic Flows. *AIAA* 93-2906.

Meslem, A., A. Dia, C. Beghein, M. E. Hassan, I. Nastase and P. J. Vialle (2011b). A comparison of three turbulence models for the prediction of parallel lobed jets in perforated panel optimization. *Building and Environment* 46(11), 2203-2219.

Meslem, A., F. Bode, I. Nastase and O. Martin (2012). Optimization of lobed perforated panel diffuser: numerical study of orifice geometry. *Modern Applied Science* 6(12), 59.

Meslem, A., I. Nastase and F. Allard (2010). Passive mixing control for innovative air diffusion terminal devices for buildings. *Building and Environment* 45, 2679-2688.

Meslem, A., M. Elhassan and I. Nastase (2011a). Analysis of jet entrainment mechanism in the transitional regime by time-resolved PIV. *Journal of Visualization* 14, 41-52.

Meslem, A., R. Greffet, I Nastase and A. Ammar (2014). Experimental investigation of jets from rectangular six-lobed and round orifices at very low Reynolds number. *Meccanica* 49, 2419–2437.

Nastase, I., A. Meslem, V. Iordach, and I. Colda (2011). Lobed grilles for high mixing ventilation - An experimental analysis in a full scale model room. *Building and Environment* 46, 547-555.

Pratte, B.D., and J. R., Keffer (1972). The swirling turbulent jet. *J.I. of Engineerinng transactions of the Japan Society of Mechanical Engineers*, 739-748.

Yuan, Y. (2000). *Jet fluid mixing control through manipulation of inviscid flow structures*. Ph. D. Thesis, Virginia Polytechnic Institute and State University.